ACS APPLIED MATERIALS & INTERFACES

Research Article

www.acsami.org

Morphologically Controlled Synthesis of Porous Spherical and Cubic $LaMnO_3$ with High Activity for the Catalytic Removal of Toluene

Yazhou Wang,[†] Shaohua Xie,[‡] Jiguang Deng,[‡] Sixu Deng,[†] Hao Wang,*[,†] Hui Yan,[†] and Hongxing Dai[‡]

[†]College of Materials Science and Engineering, Beijing University of Technology, Beijing 100124, China

[‡]Department of Chemistry and Chemical Engineering, College of Environmental and Energy Engineering, Beijing University of Technology, Beijing 100124, China

ABSTRACT: A morphology-controlled molten salt route was developed to synthesize porous spherical $LaMnO_3$ and cubic $LaMnO_3$ nanoparticles using the as-prepared porous Mn_2O_3 spheres as template. The porous $LaMnO_3$ spheres with an average pore size of about 34.7 nm and the cubic $LaMnO_3$ nanoparticles with a good dispersion were confirmed by scanning electron microscope, transmission electron microscope, and N_2 adsorption−desorption measurements. The mechanism of morphological transformation from the porous spherical structure to the cubic particle in the molten salt was proposed. The porous spherical $LaMnO_3$ and cubic $LaMnO_3$ catalysts exhibited high catalytic performance for the combustion of toluene, and the latter performed better than the former. Under the conditions of toluene/oxygen molar ratio = 1/400 and space velocity = 20 000 h^{-1}, the temperature required for 10, 50, and 90% toluene conversion was 110, 170, and 220 °C over the cubic $LaMnO_3$ catalyst, respectively. Based on the results of X-ray photoelectron spectroscopic and hydrogen temperature-programmed reduction characterization, we deduce that the higher surface Mn^{4+}/Mn^{3+} molar ratio and better low-temperature reducibility enhanced the catalytic performance of cubic $LaMnO_3$. Taking the facile morphology-controlled synthesis and excellent catalytic performance into consideration, we believe that the well-defined morphological $LaMnO_3$ samples are good candidate catalytic materials for the oxidative removal of toluene.

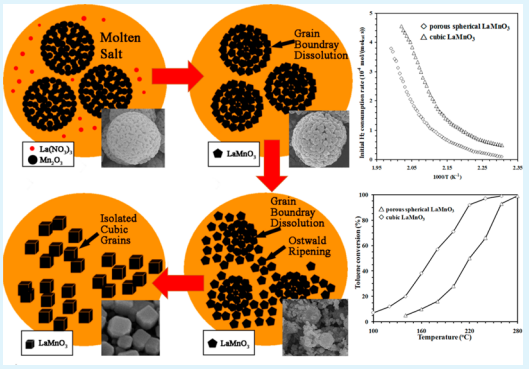

KEYWORDS: *molten salt synthesis, morphological control, lanthanum manganate catalyst, toluene combustion*

1. INTRODUCTION

Volatile organic compounds (VOCs) emitted from industrial and transportation activities are considered to be one of the most severe contaminants to human health and atmospheric environment. Catalytic combustion is one of the most efficient pathways for the removal of VOCs.[1] The key issue of such a technology is the development of highly active catalysts. Up to now, noble metal,[2] single or mixed transition metal oxide,[3] and perovskite-type oxide (ABO_3)[4] have been utilized to catalyze the combustion of VOCs. Compared to the noble metal catalysts, although ABO_3 shows inferior catalytic performance at low temperatures,[5,6] ABO_3 is much cheaper in large-scale applications[4] and shows good catalytic activities for VOCs oxidation at high temperatures.[7] $LaMnO_3$ is one of the most popular ABO_3 catalysts investigated so far. For example, $LaMnO_3$ exhibits good catalytic performance for the complete oxidation of ethanol, benzene, and toluene. However, the temperature required for achieving a 90% conversion of ethanol, benzene, or toluene ($T_{90\%}$) is relatively high. Under the conditions of ethanol/oxygen molar ratio = 1/3 and space velocity (SV) = 60 000 h^{-1}, benzene/oxygen molar ratio = 1/100, and SV = 14 100 h^{-1}, or toluene partial pressure = 192 Pa and SV = 186 h^{-1}, the corresponding $T_{90\%}$ was 202, 335, and 310 °C.[8−10] Therefore, it is highly desired to improve the catalytic performance of $LaMnO_3$ (i.e., decreasing the $T_{90\%}$ value). As we know, the catalytic activity of $LaMnO_3$ is associated with its physicochemical properties, including oxygen nonstoichiometry, surface area, morphology, and pore structure.[11−14] Recently, a number of strategies, such as solid-state method,[15] combustion method,[16] sol−gel method,[17] coprecipitation method,[18] hydrothermal synthesis,[19] and biotechnological method,[20] have been developed for the fabrication of ABO_3 with improved physicochemical properties and enhanced catalytic performance. Meanwhile, the molten salt synthesis have been employed to prepare some $LaMO_3$ (M = Mn, Co, Fe, Ni, Al, Sc, Cr, Ga, and In) with nonuniform morphology due to its lower synthesizing temperature compared with solid-state method.[21−23] However, it is rare to come across the literature related to the molten salt synthesis of $LaMnO_3$ nanostructures with high activity for the catalytic removal of VOCs.

In our previous works, we prepared polycrystalline $LaMnO_3$ nanoparticles[19] and single-crystal $La_{1-x}Sr_xMnO_3$ (x = 0.4, 0.5, 0.6) microcubes[24] via the citric acid complexing and hydro-

Received: January 23, 2014
Accepted: September 29, 2014
Published: September 29, 2014

thermal treatment combined method and hydrothermal method, respectively. The polycrystalline $LaMnO_3$ nanoparticles and single-crystal $La_{1-x}Sr_xMnO_3$ microcubes exhibited good catalytic performance for the combustion of toluene. As an extension of these studies, we herein reported the molten salt synthesis of $LaMnO_3$ with porous spherical and cubic morphologies and investigated their catalytic performance for toluene combustion.

2. EXPERIMENTAL SECTION

The porous spherical and cubic $LaMnO_3$ samples were prepared by the molten salt method. First, the porous spherical Mn_2O_3 precursor was obtained by calcining the spherical $MnCO_3$ at 600 °C for 10 h, which was prepared via a simple precipitation route using $MnSO_4{\cdot}H_2O$ as manganese source and NH_4HCO_3 as precipitant, as described in our previous study.[25] The mixture of $NaNO_3$ and KNO_3 with a molar ratio of 2:1 was adopted as the molten salt. Stoichiometric amounts of $La(NO_3)_3$ and porous spherical Mn_2O_3 were well mixed with the molten salt using ethanol as the dispersion agent, in which $La(NO_3)_3$ and Mn_2O_3 to molten salt molar ratio was of 1:20. After being dried at 80 °C, the solids were calcined in air at 550 °C for 4 and 6 h, respectively, thus obtaining the porous spherical $LaMnO_3$ and cubic $LaMnO_3$ samples.

X-ray power diffraction (XRD) measurements were carried out on a Shimadzu XRD diffractometer with Cu Kα. Morphologies and microstructures of the samples were observed using Hitachi S4800 field emission scanning electron microscope (FESEM) and JEM 2100 transmission electron microscope (TEM) with an accelerating voltage of 200 kV. Nitrogen adsorption−desorption isotherms for surface area and pore analysis were measured with an SSA-4200 (Builder Instruments) volumetric adsorption analyzer. Before measurement, the samples were outgassed under vacuum at 90 °C for 5 h. Hydrogen temperature-programmed reduction (H_2-TPR) experiments were conducted using 0.1 g of the sample in a flow (50 mL/min) of 5% H_2/Ar (balance) at a heating rate of 10 °C/min from 50 to 850 °C. The effluent was monitored by a chemical adsorption analyzer (Autochem II 2920, Micromeritics). The thermal conductivity response was calibrated against the reduction of a known CuO powder sample (Aldrich, 99.995%). The initial (no phase transformation takes place when reduction of the sample is less than 20% of the low-temperature reduction peak) H_2 consumption rate of the sample was calculated according to the H_2 consumption rate normalized per mole sample in the initial stage of the reduction peak. X-ray photoelectron spectroscopy (XPS) data were obtained using an ESCALab250 electron spectrometer (Thermo Scientific Corporation) with monochromatic 150 W Al Kα radiation. The binding energies (BEs) were referenced to the C 1s line at 284.8 eV.

The catalytic activity evaluation of the as-prepared samples was carried out in a continuous flow fixed-bed quartz microreactor (i.d. = 4 mm). The reactant feed was composed of 1000 ppm toluene, O_2, and N_2 (balance). The toluene/O_2 molar ratio was 1/400, and the SV was 20 000 h^{-1}. Reactants and products were monitored online by a gas chromatograph (GC-2010, Shimadzu). Toluene and permanent gases were separated by a stabilwax@-DA column (30 m in length) and a 1/8 in Carboxen 1000 column (3 m in length), respectively.

3. RESULTS AND DISCUSSION

The nature of the precursor template is important because it can determine the morphology of the final product in the synthesis process of $LaMnO_3$. Shown in Figure 1 are the XRD results of the as-prepared $MnCO_3$ and Mn_2O_3 precursors. The XRD peaks of the as-prepared $MnCO_3$ sample could be well indexed to the rhombohedral $MnCO_3$ phase (JCPDS card No. 41-1472).[26] After heating $MnCO_3$ at 600 °C for 10 h, the $MnCO_3$ was completely transformed into the cubic Mn_2O_3 phase (JCPDS card No. 41-1442).[27] Figure 2 shows the SEM images of the precursors. As shown in Figure 2a, the $MnCO_3$

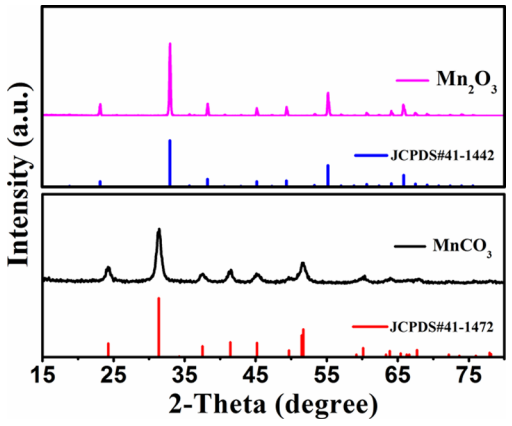

Figure 1. XRD patterns of the as-prepared $MnCO_3$ and Mn_2O_3 precursors.

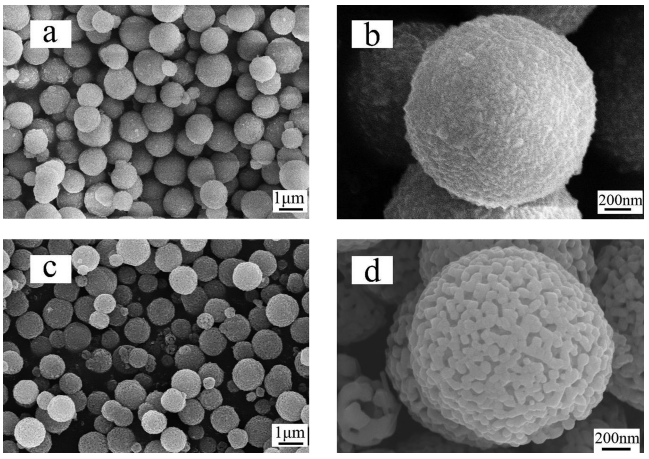

Figure 2. SEM images of the as-prepared $MnCO_3$ (a, b) and Mn_2O_3 (c, d) precursors.

powder dispalyed a uniform spherical morphology with a typical diameter of 1 μm. From the higher resolution SEM image (Figure 2b), one can see that the surface of the $MnCO_3$ spheres were constructed by closely packed nanocrystallites. After thermal treatment of $MnCO_3$ at 600 °C for 10 h, a highly porous network consisting of small Mn_2O_3 entities (50−100 nm in diameter) was obtained (Figure 2c and d). The possible formation mechanism of porous spherical Mn_2O_3 might be that some manganese oxide primary particles first crystallized as nuclei and then grew up into larger Mn_2O_3 crystallites by adsorbing surrounding primary particles via the Oswald ripening process,[28] as observed from our previous work.[25]

During the process of calcination of reactants, the Mn_2O_3 precursor was transformed into $LaMnO_3$ through reacting with $La(NO_3)_3$ in the molten salt medium. XRD patterns of the samples obtained by heating the mixture of $La(NO_3)_3$ and porous spherical Mn_2O_3 in the molten salt of $NaNO_3$ and KNO_3 at 550 °C at different intervals are shown in Figure 3. It is clearly seen that there were the Mn_2O_3 (JCPDS card No.41-1442) and $LaMnO_3$ (JCPDS card No.54-1275) phases in the sample derived at 550 °C for 1 h (Figure 3a).[11,14] With a rise in calcination time from 1 to 3 h (Figure 3b and c), the intensity of the signals due to the Mn_2O_3 phase decreased, while that attributable to the $LaMnO_3$ phase increased. All of the diffraction peaks in Figure 3d could be well indexed to the single phase of perovskite-type oxide $LaMnO_3$, and no other

dx.doi.org/10.1021/am500489x | ACS Appl. Mater. Interfaces 2014, 6, 17394−17401

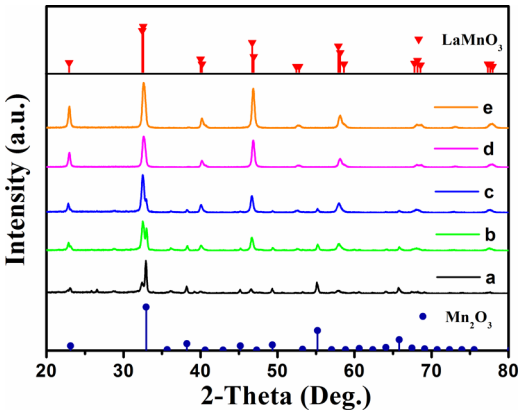

Figure 3. XRD patterns of the samples by heating the mixture of $La(NO_3)_3$ and porous spherical Mn_2O_3 in the molten salt at 550 °C for 1 h (a), 2 h (b), 3 h (c), 4 h (d), and 6 h (e).

impurities were detected. This result indicates that in the molten salt of $NaNO_3$ and KNO_3, single-phase $LaMnO_3$ could be generated from the mixture of $La(NO_3)_3$ and porous spherical Mn_2O_3 after thermal treatment at 550 °C for 4 h. In addition, a further increase in sintering time to 6 h (Figure 3e) was beneficial for the improvement of crystallinity.

The molten salt method, which plays a vital role in maintaining the morphology of the product according to the previous works,[29] was employed to synthesize the porous spherical $LaMnO_3$ from porous spherical Mn_2O_3 precursors. Figure 4 gives the SEM and TEM images of the $LaMnO_3$

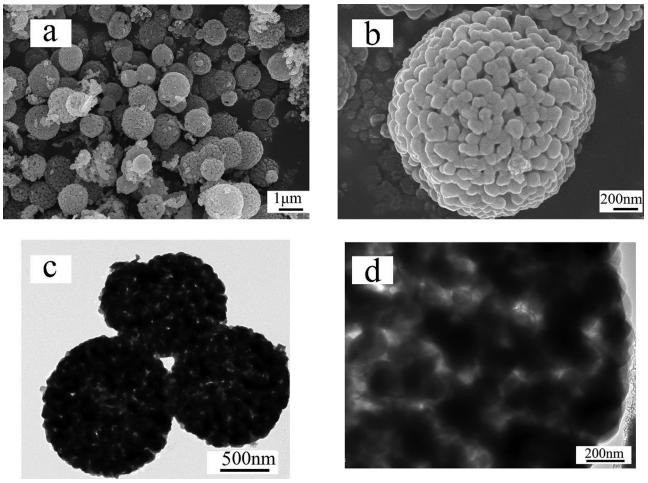

Figure 4. SEM (a, b) and TEM (c, d) images of the porous spherical $LaMnO_3$ sample obtained after calcination at 550 °C for 4 h.

sample obtained after calcination at 550 °C for 4 h. Clearly, the porous spherical structure of the Mn_2O_3 precursor did not collapse and agglomerate and was well retained during the calcination process. The as-obtained $LaMnO_3$ spheres were composed of aggregated nanocrystallites with irregularly shaped pores among them. The size of the nanoparticles was in the range 50−100 nm, which was slightly larger than that of the original Mn_2O_3 nanocrystallites, and the size of the pores became smaller due to the growth of the primary nanocrystallites. TEM images (Figure 4c and d) further show that these pores existed not only on the surface but also within the $LaMnO_3$ spheres. We deduce that the preservation of a porous spherical structure was due to the "template formation" mechanism, where $La(NO_3)_3$ is much more soluble than porous spherical Mn_2O_3 in the molten salt at 550 °C. In this case, $La(NO_3)_3$ primarily dissolved into the salt and then diffused onto the surface of the less soluble Mn_2O_3 precursor and in situ reacted to form the $LaMnO_3$ phase.[30] As a result, the morphology of the $LaMnO_3$ powder retains the porous spherical structure of the less soluble Mn_2O_3.

It is interesting to notice that after 5 h calcination, the spherical morphology was gradually smashed, as observed from the SEM image of the $LaMnO_3$ powder in Figure 5. From

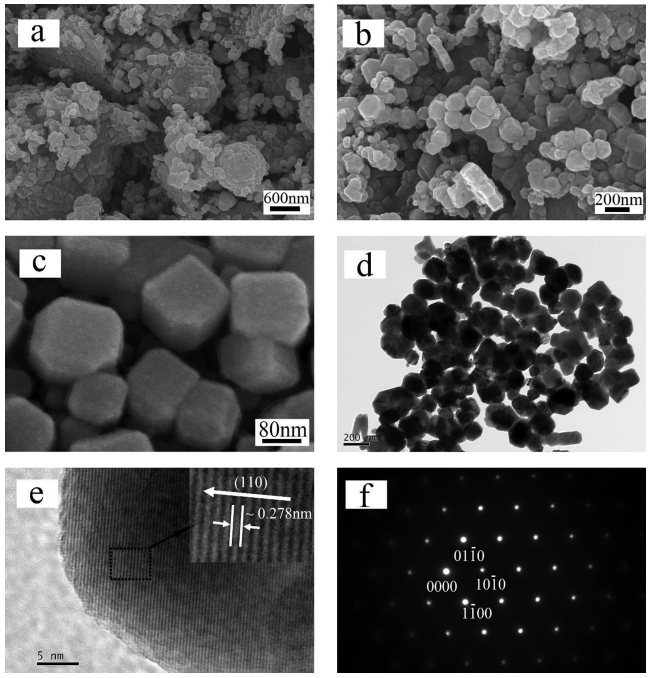

Figure 5. SEM image (a) of the $LaMnO_3$ sample obtained after calcination at 550 °C for 5 h; SEM (b, c), TEM (d), and HRTEM (e) images as well as the SAED pattern (f) of the cubic $LaMnO_3$ sample obtained after calcination at 550 °C for 6 h.

Figure 5a, one can see that only a few porous $LaMnO_3$ spheres were preserved, while most of them were broken into nanocrystallites. The diameter of the residual $LaMnO_3$ spheres decreased obviously, indicating that the nanocrystallites were generated by peeling from the surface to the core of the $LaMnO_3$ spheres. Shown in Figure 5b and c are the SEM images of the $LaMnO_3$ powder obtained at 550 °C for 6 h. It can be found that the powder was mainly composed of cubic particles. The edge of the cubic $LaMnO_3$ particles was in the range 100−150 nm. The TEM image (Figure 5d) confirms the cubic morphology of the particles. As can be seen from the HRTEM image (Figure 5d), the lattice spacing was calculated to be ca. 0.278 nm, in good consistence with that (0.277 nm) of the (110) plane of the $LaMnO_3$ crystal (JCPDS card No. 54-1275). In the selected-area electron diffraction (SAED) pattern (Figure 5f), there were regularly aligned lines of sharp diffraction spots, indicating that the cubic $LaMnO_3$ particles were single-crystal.

A possible mechanism of the morphological transformation from the porous spherical structure to the cubic particle in the molten salt is proposed, as illustrated in Figure 6. First, the as-prepared porous Mn_2O_3 spheres, $La(NO_3)_3$, and $NaNO_3$−

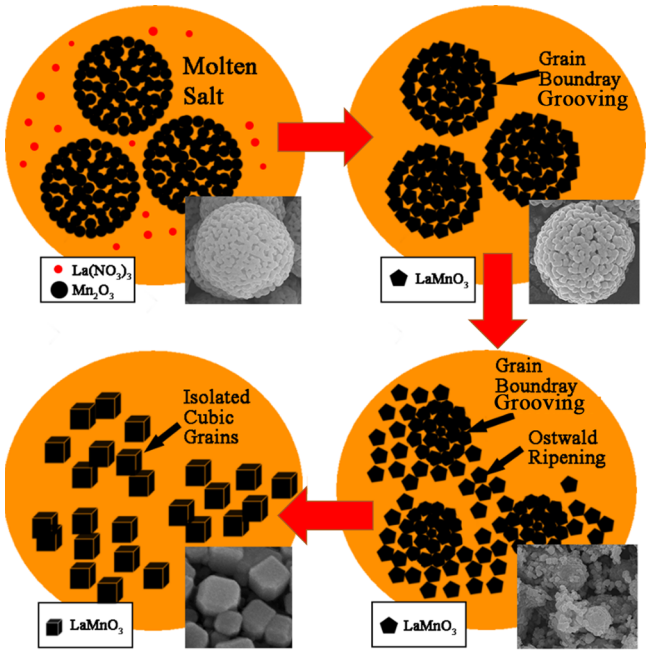

Figure 6. Mechanism of the morphological transformation of $LaMnO_3$ from the porous spherical structure to the cubic particle in the molten salt.

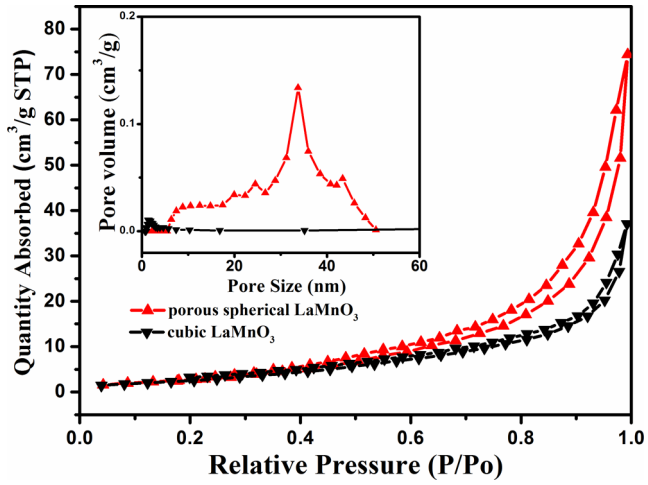

Figure 7. Nitrogen adsorption−desorption isotherms and pore size distributions of the porous spherical $LaMnO_3$ and cubic $LaMnO_3$ samples.

KNO_3 were well mixed, and put into the ceramic crucible at room temperature. The well mixed powders were heated at a constant rate in a muffle furnace to the melting point of $NaNO_3$−KNO_3 flux (550 °C). The molten salt of the $NaNO_3$−KNO_3 flux served as a solvent for the reaction between the porous Mn_2O_3 spheres and $La(NO_3)_3$. Compared with the porous Mn_2O_3 spheres, $La(NO_3)_3$ could be readily dissolved in the molten salt. In other words, $La(NO_3)_3$ could easily migrate into the porous Mn_2O_3 spheres, while the porous Mn_2O_3 spheres acted as the template. After reaction at 550 °C for 4 h, all of the porous Mn_2O_3 spheres and $La(NO_3)_3$ were changed into the porous $LaMnO_3$ spheres (Figures 3 and 4). With a further rise in reaction time from 4 to 5 h, due to the grain boundary grooving and dissolution in the molten salt, the aggregated nanocrysallites on the surface of the porous $LaMnO_3$ spheres gradually disintegrated into individual grains. Similar phenomena were also observed in the synthesis of $BaTiO_3$ nanostructures and $Na_{0.5}Bi_{0.5}TiO_3$−$BaTiO_3$ whiskers.[31,32] After calcination at 550 °C for 6 h, the porous $LaMnO_3$ spheres were totally broken into individual grains. Via the Oswald ripening process in the molten salt, the grains gradually grew into the single-crystal cubic particles (Figure 5).

Figure 7 shows the N_2 adsorption−desorption isotherms and pore size distributions of the porous spherical $LaMnO_3$ and cubic $LaMnO_3$ samples. It can be seen that the samples exhibited similar N_2 adsorption−desorption isotherms, which could be ascribed to type V isotherm. The N_2 adsorption quantity of porous spherical $LaMnO_3$ was much higher than that of cubic $LaMnO_3$, indicating that there were abundance pores in the former sample, in agreement with the SEM and TEM results. In addition, the porous spherical $LaMnO_3$ sample displayed a type H3 hysteresis loop, which was commonly observed in the agglomerate solids with slit-shaped pores.[33] Actually, the porous structure might be generated from the aggregation of nonuniform nanoparticles in $LaMnO_3$. However, the hysteresis loop of the cubic $LaMnO_3$ sample was not obvious. Surface areas of the porous spherical $LaMnO_3$ and cubic $LaMnO_3$ samples were 28 and 11 m^2/g, respectively.

The XPS technique was used to investigate the surface properties of the porous spherical and cubic $LaMnO_3$ samples. According to the La 3d (not shown) and Mn 2p XPS spectra, we calculated the surface La/Mn molar ratios (1.40 and 1.47 on the porous spherical and cubic $LaMnO_3$ samples, respectively) and found that there was La enrichment on the $LaMnO_3$ surface. The Mn $2p_{3/2}$XPS spectra of the as-prepared samples are shown in Figure 8a. The peak at BE = 642.2 eV could be decomposed into two components at BE = 642.1 and 643.1 eV, which were attributable to the surface Mn^{3+} and Mn^{4+} species,[34,35] respectively. The surface Mn^{4+}/Mn^{3+} molar ratio of porous spherical $LaMnO_3$ was 0.84, while that of cubic $LaMnO_3$ was 0.98. In other words, the average oxidation states (AOS) of manganese were 3.46 and 3.49 on the surface of the porous spherical and cubic $LaMnO_3$ samples, respectively. Due to the interaction between the 3s-core hole generated in a XPS process and 3d electrons, the 3s core levels of the 3d transition metals could exhibit exchange splitting. The splitting magnitude of Mn 3s spectra was associated with the valence state of Mn ions. The expected splitting of the 3s level is about 6.5, 5.5, and 4.5 eV for Mn^{2+}, Mn^{3+}, and Mn^{4+}, respectively. In the present study, the corresponding Mn 3s multiple splitting value was 4.98 and 4.86 eV for the porous spherical and cubic $LaMnO_3$ samples (Figure 8b), confirming that the AOSs of the surface manganese species were about 3.4,[36−39] as revealed from the Mn $2p_{3/2}$ spectra of the samples. As shown in Figure 8c, the O 1s XPS peak could be decomposed into three components at BE = 529.5, 531.6, and 533.4 eV, which were ascribable to the surface lattice oxygen (O_{latt}), adsorbed oxygen (O_{ads}, such as O^-, O^{2-}, or O_2^{2-}), and hydrated oxide species,[40,41] respectively. The surface O_{ads}/O_{latt} molar ratio of the porous spherical $LaMnO_3$ sample was 1.91, while that of the cubic $LaMnO_3$ sample was 1.32.

Under the conditions of toluene/O_2 molar ratio = 1/400 and SV = 20 000 h^{-1}, no conversion of toluene was observed below 400 °C over quartz sands (not shown). That is to say, there was no occurrence of homogeneous reactions in the present study. Over the porous spherical $LaMnO_3$ and cubic $LaMnO_3$ samples, toluene conversion increased with a rise in reaction temperature (Figure 9a). It should be mentioned that toluene

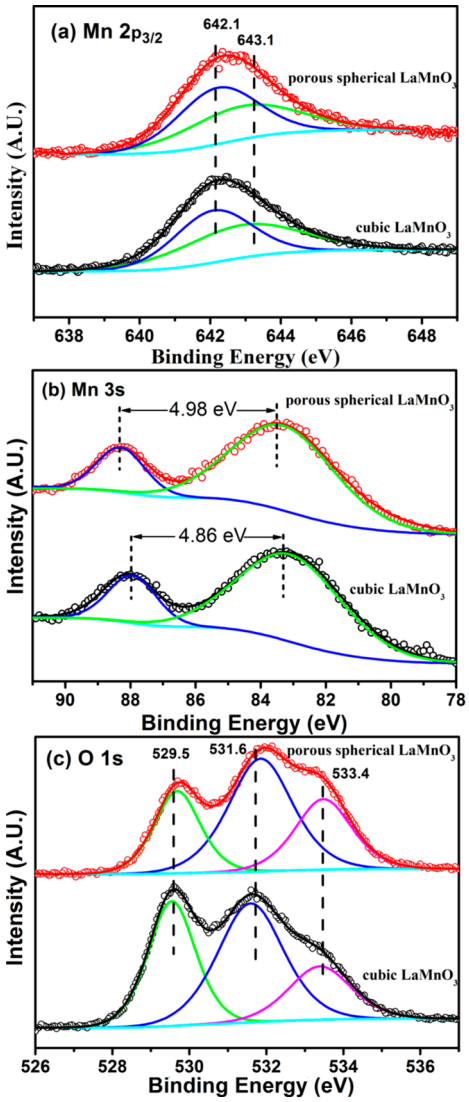

Figure 8. Mn $2p_{3/2}$ (a), Mn 3s (b), and O 1s (c) XPS spectra of the porous spherical $LaMnO_3$ and cubic $LaMnO_3$ samples.

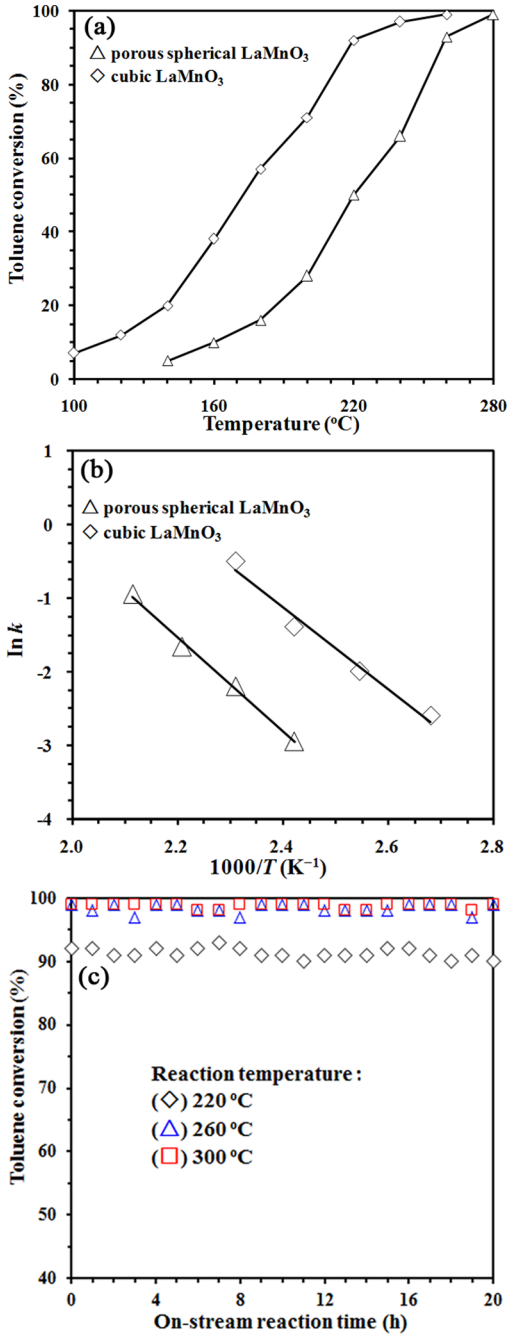

Figure 9. (a) Toluene conversion versus reaction temperature over the porous spherical $LaMnO_3$ and cubic $LaMnO_3$ catalysts under the conditions of toluene concentration = 1000 ppm, toluene/O_2 molar ratio = 1/400, and SV = 20 000 h^{-1}; (b) Arrhenius plots for toluene oxidation over the as-prepared $LaMnO_3$ catalysts; and (c) catalytic activity as a function of on-stream reaction time over the cubic $LaMnO_3$ sample for toluene oxidation under the conditions of toluene concentration = 1000 ppm, toluene/O_2 molar ratio = 1/400, reaction temperature = 220, 260, and 300 °C, and SV = 20 000 h^{-1}.

was completely oxidized into CO_2 and H_2O over the as-prepared $LaMnO_3$ samples, and no incomplete oxidation products were detected in the oxidation of toluene. The $T_{10\%}$, $T_{50\%}$, and $T_{90\%}$ (temperatures required for achieving 10, 50, and 90% toluene conversions, respectively) over porous spherical $LaMnO_3$ were 160, 220, and 258 °C, whereas those over cubic $LaMnO_3$ were 110, 170, and 220 °C, respectively. We ever reported that under the same conditions, the $T_{10\%}$, $T_{50\%}$, and $T_{90\%}$ were 210, 275, and 298 °C over polycrystalline $LaMnO_3$ nanoparticles (surface area = 27 m^2/g) obtained using the combined method of citric acid complexing and hydrothermal processing,[19] and 209, 250, and 254 °C over single-crystal $La_{0.5}Sr_{0.5}MnO_3$ microcubes (surface area = 1.8 m^2/g) obtained via the hydrothermal route.[24] Obviously, the porous spherical $LaMnO_3$ and cubic $LaMnO_3$ samples performed much better than the polycrystalline $LaMnO_3$ nanoparticles[19] and single-crystal $La_{0.5}Sr_{0.5}MnO_3$ microcubes.[24] According to our previous studies,[13,14] in the case of excessive oxygen, toluene oxidation would follow a first order reaction mechanism with respect to toluene concentration (c, μmol/g): $r = -kc = (-A \exp(-E_a/RT))c$, where r is the reaction rate (μmol/(g s)), k the rate constant (s^{-1}), A the pre-exponential factor, and E_a the apparent activation energy (kJ/mol). The k values can be calculated from the reaction rates and reactant conversions at different temperatures. Shown in Figure 9b are the Arrhenius plots for the oxidation of toluene over the as-prepared $LaMnO_3$ catalysts. The k and E_a values for toluene oxidation over the $LaMnO_3$ catalysts could be obtained according to the slopes of the Arrhenius plots, and the results are summarized in Table 1.

dx.doi.org/10.1021/am500489x | ACS Appl. Mater. Interfaces 2014, 6, 17394−17401

Table 1. Rate Constants (k), Apparent Activation Energies (E_a), and Correlation Coefficients (R^2) of the Plot ln k versus Inverse Temperature for Toluene Oxidation over the Present $LaMnO_3$ Catalysts

	k (s^{-1})							
catalyst	140 °C	160 °C	180 °C	200 °C	220 °C	240 °C	E_a (kJ/mol)	R^2
porous spherical $LaMnO_3$	0.05	0.11	0.19	0.39	1.0	1.94	53 ± 0.53	0.99
cubic $LaMnO_3$	0.25	0.61	1.32	2.45	11.5	32.3	46 ± 0.92	0.98

It is observed that for each catalyst, the k value increased with the rise in temperature. However, the k values for the cubic $LaMnO_3$ catalyst were much higher than those for the porous spherical $LaMnO_3$ catalyst. The E_a value (46 ± 0.92 kJ/mol) of the cubic $LaMnO_3$ catalyst was lower than that (53 ± 0.53 kJ/mol) of the porous spherical $LaMnO_3$ catalyst. To examine the catalytic stability, we carried out on-stream reaction experiment over the cubic $LaMnO_3$ sample at 220 °C (where ca. 90% toluene conversion was achieved), 260 °C (where a maximum toluene conversion was achieved), and 300 °C (a temperature lower than the calcination temperature during the preparation of cubic $LaMnO_3$), and the result is shown in Figure 9c. It is found that there was no significant drop in catalytic activity within 20 h of on-stream reaction. In other words, the cubic $LaMnO_3$ sample was catalytically durable.

Although the surface area of cubic $LaMnO_3$ was lower than that of porous spherical $LaMnO_3$, the former catalyst performed better than the latter one. In other words, the surface area exerted negligible influence on catalytic performance of the present catalysts for toluene oxidation. As we know, the redox cycles of B ions (from a higher oxidation state to a lower oxidation state, and vice versa) in ABO_3 played an important role in enhancing catalytic performance for the oxidation of organic compounds.[42] In the case of $LaMnO_3$, catalytic activity might be associated with the extent of the $Mn^{4+} \Leftrightarrow Mn^{3+}$ redox process. It is well-known that oxidation reaction takes place on the surface of a catalyst. That is to say, the surface composition of a catalyst could influence its catalytic performance. The surface Mn^{4+}/Mn^{3+} molar ratio (0.98) of cubic $LaMnO_3$ was higher than that (0.84) of porous spherical $LaMnO_3$. A higher surface Mn^{4+}/Mn^{3+} molar ratio was beneficial for enhancing the redox cycles of Mn ions, thus improving the catalytic activity. Shown in Figure 10a are the H_2-TPR profiles of the porous spherical $LaMnO_3$ and cubic $LaMnO_3$ samples. Apparently, the reduction of the two samples could be divided into two regions:[43,44] (i) in the low-temperature region (room temperature to 500 °C), Mn^{4+} ions were reduced to Mn^{3+} ions, and partial surface Mn^{3+} ions were reduced to Mn^{2+} ions; (ii) in the high-temperature region (>500 °C), the bulk Mn^{3+} ions were reduced to Mn^{2+} ions. The actual H_2 consumption of porous spherical $LaMnO_3$ and cubic $LaMnO_3$ was 2.15 and 2.30 mmol/g_{cat}, respectively. As mentioned above, all of the Mn ions were reduced to Mn^{2+}. Based on the actual H_2 consumption, the AOS of Mn in porous spherical $LaMnO_3$ and cubic $LaMnO_3$ was estimated to be 3.04 and 3.11, respectively. Obviously, the AOSs (3.04−3.11) of Mn in the bulk were lower than those (3.46−3.49) of Mn on the surface. In the present study, oxidation of toluene over porous spherical $LaMnO_3$ and cubic $LaMnO_3$ was completed below 280 °C. Therefore, we deduce that catalytic performance of the as-prepared catalysts might be mainly dependent on their low-temperature reducibility, which could be evaluated using the initial hydrogen consumption rate. As can be seen from Figure 10b, the initial hydrogen consumption rate of cubic $LaMnO_3$ was higher than that of porous spherical $LaMnO_3$, coinciding with the sequence of their catalytic performance.

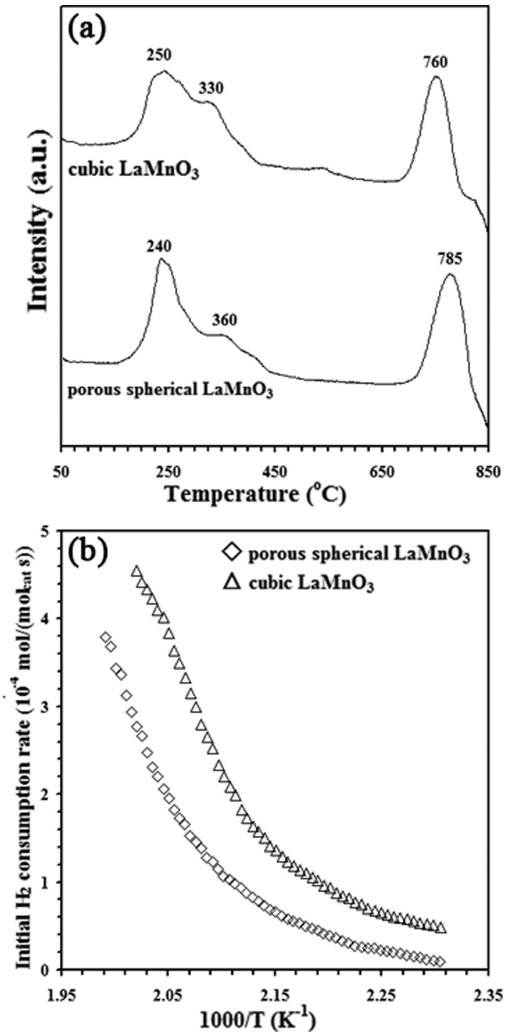

Figure 10. (a) TPR profiles and (b) initial hydrogen consumption rate as a function of the reciprocal of temperature of the porous spherical $LaMnO_3$ and cubic $LaMnO_3$ catalysts.

4. CONCLUSION

By adopting the molten salt method, we prepared the porous spherical $LaMnO_3$ and cubic $LaMnO_3$ samples. The morphological transformation from the porous spherical structure to cubic particles in the molten salt was explained by "template formation" and "grain boundary grooving and dissolution followed by the Oswald ripening process" mechanism. Under the condition of toluene concentration = 1000 ppm, toluene/O_2 molar ratio = 1/400, and SV = 20 000 h^{-1}, the porous spherical $LaMnO_3$ and cubic $LaMnO_3$ samples exhibited good catalytic activities for the combustion of toluene, in which the cubic $LaMnO_3$ sample performed better than the porous

dx.doi.org/10.1021/am500489x | ACS Appl. Mater. Interfaces 2014, 6, 17394−17401

spherical $LaMnO_3$ sample. The $T_{10\%}$, $T_{50\%}$, and $T_{90\%}$ for toluene combustion over cubic $LaMnO_3$ were 110, 170, and 220 °C, respectively. It is concluded that the low-temperature reducibility and surface Mn^{4+}/Mn^{3+} molar ratio of cubic $LaMnO_3$ played an important role in determining the catalytic performance.

AUTHOR INFORMATION

Corresponding Author

*Fax: +86-10-6739-2733. Email: haowang@bjut.edu.cn.

Notes

The authors declare no competing financial interest.

ACKNOWLEDGMENTS

This work was supported by the Foundation on the Creative Research Team Construction Promotion Project of Beijing Municipal Institutions and the National Natural Science Foundation of China (21103005).

REFERENCES

(1) Li, W. B.; Wang, J. X.; Gong, H. Catalytic Combustion of VOCs on Non-Noble Metal Catalysts. *Catal. Today* **2009**, *148*, 81−87.

(2) Ruud W, v. d. B.; Louw, R.; Mulder, P. Formation of Polychlorinated Benzenes During The Catalytic Combustion of Chlorobenzene Using a Pt/γ-Al_2O_3 Catalyst. *Appl. Catal., B* **1998**, *16*, 219−226.

(3) Sinha, A. K.; Suzuki, K. Novel Mesoporous Chromium Oxide for VOCs Elimination. *Appl. Catal., B* **2007**, *70*, 417−422.

(4) Blasin-Aubé, V.; Belkouch, J.; Monceaux, L. General Study of Catalytic Oxidation of Various VOCs over $La_{0.8}Sr_{0.2}MnO_{3+x}$ Perovskite Catalyst—Influence of Mixture. *Appl. Catal., B* **2003**, *43*, 175−186.

(5) Giraudon, J.-M.; Elhachimi, A.; Leclercq, G. Catalytic Oxidation of Chlorobenzene over Pd/Perovskites. *Appl. Catal., B* **2008**, *84*, 251−261.

(6) Blanco, J.; Petre, A.; Yates, M.; Martin, M.; Martin, J.; Martin-Luengo, M. Tailor-Made High Porosity VOC Oxidation Catalysts Prepared by a Single-Step Procedure. *Appl. Catal., B* **2007**, *73*, 128−134.

(7) Varma, S.; Wani, B.; Gupta, N. Synthesis, Characterisation, TPR/TPO, and Activity Studies on $LaMnxV_{1-x}O_{4-\delta}$ Catalysts. *Appl. Catal., A* **2001**, *205*, 295−304.

(8) Najjar, H.; Batis, H. La−Mn Perovskite-Type Oxide Prepared by Combustion Method: Catalytic Activity in Ethanol Oxidation. *Appl. Catal., A* **2010**, *383*, 192−201.

(9) Irusta, S.; Pina, M.; Menendez, M.; Santamarıa, J. Catalytic Combustion of Volatile Organic Compounds over La-Based Perovskites. *J. Catal.* **1998**, *179*, 400−412.

(10) Spinicci, R.; Faticanti, M.; Marini, P.; De Rossi, S.; Porta, P. Catalytic Activity of $LaMnO_3$ and $LaCoO_3$ Perovskites Towards VOCs Combustion. *J. Mol. Catal. A: Chem.* **2003**, *197*, 147−155.

(11) Liu, Y.; Dai, H.; Du, Y.; Deng, J.; Zhang, L.; Zhao, Z. Lysine-Aided PMMA-Templating Preparation and High Performance of Three-Dimensionally Ordered Macroporous $LaMnO_3$ with Mesoporous Walls for The Catalytic Combustion of Toluene. *Appl. Catal., B* **2012**, *119*−*120*, 20−31.

(12) Liu, Y.; Dai, H.; Du, Y.; Deng, J.; Zhang, L.; Zhao, Z.; Au, C. T. Controlled Preparation and High Catalytic Performance of Three-Dimensionally Ordered Macroporous $LaMnO_3$ with Nanovoid Skeletons for The Combustion of Toluene. *J. Catal.* **2012**, *287*, 149−160.

(13) Spinicci, R.; Delmastro, A.; Ronchetti, S.; Tofanari, A. Catalytic Behaviour of Stoichiometric and Non-Stoichiometric $LaMnO_3$ Perovskite Towards Methane Combustion. *Mater. Chem. Phys.* **2003**, *78*, 393−399.

(14) Hou, T.; Yang, H.; Fan, X.; Zhang, X. Catalytic Oxidation of Ammonia to NO over Perovskite-Type $LaMnO_3$ and $LaVO_4$ Catalysts. *Catal. Lett.* **2011**, *141*, 1215−1218.

(15) Kuhn, J. N.; Ozkan, U. S. Surface Properties of Sr- and Co-Doped $LaFeO_3$. *J. Catal.* **2008**, *253*, 200−211.

(16) Chen, W.; Hong, J.; Li, Y. Facile Fabrication of Perovskite Single-Crystalline $LaMnO_3$ Nanocubes via a Salt-Assisted Solution Combustion Process. *J. Alloy. Compd.* **2009**, *484*, 846−850.

(17) Ciambelli, P.; Cimino, S.; De Rossi, S.; Faticanti, M.; Lisi, L.; Minelli, G.; Pettiti, I.; Porta, P.; Russo, G.; Turco, M. $AMnO_3$(A = La, Nd, Sm) and $Sm_{1-x}Sr_xMnO_3$ Perovskites as Combustion Catalysts: Structural, Redox, and Catalytic Properties. *Appl. Catal., B* **2000**, *24*, 243−253.

(18) Machocki, A.; Ioannides, T.; Stasinska, B.; Gac, W.; Avgouropoulos, G.; Delimaris, D.; Grzegorczyk, W.; Pasieczna, S. Manganese−Lanthanum Oxides Modified with Silver for The Catalytic Combustion of Methane. *J. Catal.* **2004**, *227*, 282−296.

(19) Deng, J.; Zhang, L.; Dai, H.; He, H.; Au, C. T. Strontium-Doped Lanthanum Cobaltite and Manganite: Highly Active Catalysts for Toluene Complete Oxidation. *Ind. Eng. Chem. Res.* **2008**, *47*, 8175−8183.

(20) Cyganiuk, A.; Klimkiewicz, R.; Olejniczak, A.; Lukaszewicz, J. P. Biotechnological Fabrication of $LaMnO_3$-Carbon Catalyst for N-Butanol Conversion to Ketones. *Carbon* **2010**, *48*, 99−106.

(21) Vradman, L.; Zana, J.; Kirschner, A.; Herskowitz, M. Synthesis of $LaMnO_3$ in Molten Chlorides: Effect of Preparation Conditions. *Phys. Chem. Chem. Phys.* **2013**, *15*, 10914−10920.

(22) Yang, J.; Li, R.; Zhou, J.; Li, X.; Zhang, Y.; Long, Y.; Li, Y. Synthesis of $LaMO_3$ (M = Fe, Co, Ni) Using Nitrate or Nitrite Molten Salts. *J. Alloy. Compd.* **2010**, *508*, 301−308.

(23) Kojima, T.; Nomura, K.; Miyazaki, Y.; Tanimoto, K. Synthesis of Various $LaMO_3$ Perovskites in Molten Carbonates. *J. Am. Ceram. Soc.* **2006**, *89*, 3610−3616.

(24) Deng, J.; Zhang, L.; Dai, H.; He, H.; Au, C. T. Hydrothermally Fabricated Single-Crystalline Strontium-Substituted Lanthanum Manganite Microcubes for The Catalytic Combustion of Toluene. *J. Mol. Catal. A: Chem.* **2009**, *299*, 60−67.

(25) Wang, Y.; Shao, X.; Xu, H.; Xie, M.; Deng, S.; Wang, H.; Liu, J.; Yan, H. Facile Synthesis of Porous $LiMn_2O_4$ Spheres as Cathode Materials for High-Power Lithium Ion Batteries. *J. Power Sources* **2013**, *226*, 140−148.

(26) Uchiyama, H.; Hosono, E.; Zhou, H.; Imai, H. Three-Dimensional Architectures of Spinel-Type $LiMn_2O_4$ Prepared from Biomimetic Porous Carbonates and Their Application to A Cathode for Lithium-Ion Batteries. *J. Mater. Chem.* **2009**, *19*, 4012−4016.

(27) Javed, Q.; Wang, F. P.; Rafique, M. Y.; Toufiq, A. M.; Li, Q. S.; Mahmood, H.; Khan, W. Diameter-Controlled Synthesis of α-Mn_2O_3 Nanorods and Nanowires with Enhanced Surface Morphology and Optical Properties. *Nanotechnology* **2012**, *23*, 415603.

(28) Yu, C.; Zhang, L.; Shi, J.; Zhao, J.; Gao, J.; Yan, D. A Simple Template-Free Strategy to Synthesize Nanoporous Manganese and Nickel Oxides with Narrow Pore Size Distribution, and Their Electrochemical Properties. *Adv. Funct. Mater.* **2008**, *18*, 1544−1554.

(29) Li, Z.; Lee, W. E.; Zhang, S. Low-Temperature Synthesis of $CaZrO_3$ Powder from Molten Salts. *J. Am. Ceram. Soc.* **2007**, *90*, 364−368.

(30) Cai, Z.; Xing, X.; Yu, R.; Sun, X.; Liu, G. Morphology-Controlled Synthesis of Lead Titanate Powders. *Inorg. Chem.* **2007**, *46*, 7423−7427.

(31) Maurya, D.; Petkov, V.; Kumar, A.; Priya, S. Nanostructured Lead-Free Ferroelectric $Na_{0.5}Bi_{0.5}TiO_3$−$BaTiO_3$ Whiskers: Synthesis Mechanism and Structure. *Dalton Trans.* **2012**, *41*, 5643−5652.

(32) Huang, K.-C.; Huang, T.-C.; Hsieh, W.-F. Morphology-Controlled Synthesis of Barium Titanate Nanostructures. *Inorg. Chem.* **2009**, *48*, 9180−9184.

(33) Leofanti, G.; Padovan, M.; Tozzola, G.; Venturelli, B. Surface Area and Pore Texture of Catalysts. *Catal. Today* **1998**, *41*, 207−219.

(34) Niu, J.; Deng, J.; Liu, W.; Zhang, L.; Wang, G.; Dai, H.; He, H.; Zi, X. Nanosized Perovskite-Type Oxides $La_{1-x}Sr_xMO_{3-\delta}$ (M = Co, Mn; x = 0, 0.4) for The Catalytic Removal of Ethylacetate. *Catal. Today* **2007**, *126*, 420−429.

(35) Carver, J. C.; Schweitzer, G. K.; Carlson, T. A. Use of X-ray Photoelectron Spectroscopy to Study Bonding in Cr, Mn, Fe, and Co Compounds. *J. Chem. Phys.* **1972**, *57*, 973−982.
(36) Laassiri, S.; Bion, N.; Duprez, D.; Royer, S.; Alamdari, H. Clear Microstructure−Performance Relationships in Mn-Containing Perovskite and Hexaaluminate Compounds Prepared by Activated Reactive Synthesis. *Phys. Chem. Chem. Phys.* **2014**, *16*, 4050−4060.
(37) Najjar, H.; Lamonier, J.-F.; Mentré, O.; Giraudon, J.-M.; Batis, H. Optimization of the Combustion Synthesis towards Efficient $LaMnO_{3+y}$ Catalysts in Methane Oxidation. *Appl. Catal., B* **2011**, *106*, 149−159.
(38) Zhou, X.; Xue, J.; Zhou, D.; Wang, Z.; Bai, Y.; Wu, X.; Liu, X.; Meng, J. Mn Valence, Magnetic, and Electrical Properties of $LaMnO_{3+\delta}$ Nanofibers by Electrospinning. *ACS Appl. Mater. Interfaces* **2010**, *2*, 2689−2693.
(39) Najjar, H.; Lamonier, J.-F.; Mentré, O.; Giraudon, J.-M.; Batis, H. Combustion Synthesis of $LaMn_{1-x}Al_xO_{3+\delta}$ ($0 \leq x \leq 1$): Tuning Catalytic Properties for Methane Deep Oxidation. *Catal. Sci. Technol.* **2013**, *3*, 1002−1016.
(40) Kim, M.-G.; Kim, H. S.; Ha, Y.-G.; He, J.; Kanatzidis, M. G.; Facchetti, A.; Marks, T. J. High-Performance Solution-Processed Amorphous Zinc−Indium−Tin Oxide Thin-Film Transistors. *J. Am. Chem. Soc.* **2010**, *132*, 10352−10364.
(41) Deng, H.; Lin, L.; Sun, Y.; Pang, C.; Zhuang, J.; Ouyang, P.; Li, Z.; Liu, S. Perovskite-Type Oxide $LaMnO_3$: An Efficient and Recyclable Heterogeneous Catalyst for the Wet Aerobic Oxidation of Lignin to Aromatic Aldehydes. *Catal. Lett.* **2008**, *126*, 106−111.
(42) Wu, Y.; Yu, T.; Dou, B.; Wang, C.; Xie, X.; Yu, Z.; Fan, S.; Fan, Z.; Wang, L. A Comparative Study on Perovskite-Type Mixed Oxide Catalysts $A'_xA_{1-x}BO_{3-\lambda}$ (A′ = Ca, Sr, A = La, B = Mn, Fe, Co) for NH_3 Oxidation. *J. Catal.* **1989**, *120*, 88−107.
(43) Ponce, S.; Peña, M. A.; Fierro, J. L. G. Surface Properties and Catalytic Performance in Methane Combustion of Sr-Substituted Lanthanum Manganites. *Appl. Catal., B* **2000**, *24*, 193−205.
(44) Lisi, L.; Bagnasco, G.; Ciambelli, P.; De Rossi, S.; Porta, P.; Russo, G.; Turco, M. Perovskite-Type Oxides: II. Redox Properties of $LaMn_{1-x}Cu_xO_3$ and $LaCo_{1-x}Cu_xO_3$ and Methane Catalytic Combustion. *J. Solid State Chem.* **1999**, *146*, 176−183.